Quantitative assessment of passive electrical properties of the cardiac T-tubular system by FRAP microscopy

M. Scardigli[a,b], C. Crocini[a,b], C. Ferrantini[c], T. Gabbrielli[a], L. Silvestri[a,b], R. Coppini[d], C. Tesi[c], E. A. Rog-Zielinska[e,f], P. Kohl[e,f], E. Cerbai[d], C. Poggesi[c], F. S. Pavone[a,b,g], and L. Sacconi[a,b,1]

[a]European Laboratory for Non-Linear Spectroscopy, 50019 Sesto Fiorentino, Italy; [b]National Institute of Optics, National Research Council, 50019 Sesto Fiorentino, Italy; [c]Division of Physiology, Department of Experimental and Clinical Medicine, University of Florence, 50121 Florence, Italy; [d]Division of Pharmacology, Dipartimento di Neuroscienze, Psicologia, Area del Farmaco e Salute del Bambino, University of Florence, 50139 Florence, Italy; [e]Institute for Experimental Cardiovascular Medicine, University Heart Center Freiburg–Bad Krozingen, Faculty of Medicine, University of Freiburg, 79110 Freiburg, Germany; [f]The Magdi Yacoub Institute, National Heart and Lung Institute, Imperial College London, UB9 6JH London, United Kingdom; and [g]Department of Physics and Astronomy, University of Florence, 50019 Florence, Italy

Edited by Clara Franzini-Armstrong, University of Pennsylvania Medical Center, Philadelphia, PA, and approved April 14, 2017 (received for review February 9, 2017)

Well-coordinated activation of all cardiomyocytes must occur on every heartbeat. At the cell level, a complex network of sarcolemmal invaginations, called the transverse-axial tubular system (TATS), propagates membrane potential changes to the cell core, ensuring synchronous and uniform excitation–contraction coupling. Although myocardial conduction of excitation has been widely described, the electrical properties of the TATS remain mostly unknown. Here, we exploit the formal analogy between diffusion and electrical conductivity to link the latter with the diffusional properties of TATS. Fluorescence recovery after photobleaching (FRAP) microscopy is used to probe the diffusion properties of TATS in isolated rat cardiomyocytes: A fluorescent dextran inside TATS lumen is photobleached, and signal recovery by diffusion of unbleached dextran from the extracellular space is monitored. We designed a mathematical model to correlate the time constant of fluorescence recovery with the apparent diffusion coefficient of the fluorescent molecules. Then, apparent diffusion is linked to electrical conductivity and used to evaluate the efficiency of the passive spread of membrane depolarization along TATS. The method is first validated in cells where most TATS elements are acutely detached by osmotic shock and then applied to probe TATS electrical conductivity in failing heart cells. We find that acute and pathological tubular remodeling significantly affect TATS electrical conductivity. This may explain the occurrence of defects in action potential propagation at the level of single T-tubules, recently observed in diseased cardiomyocytes.

cardiac disease | transverse-axial tubular system | diffusion | electrical conductivity | porous rock

The sequential and coherent recruitment of all cardiomyocytes that occurs on every heartbeat is fundamental for proper contraction of the heart. Every heartbeat is triggered by a depolarizing event, the action potential (AP), spontaneously generated in cardiac pacemaker cells, which propagates through the conductive tissue and the working myocardium. The well-coordinated activation of all cardiomyocytes involves a spreading AP wave, conducted from cell to cell throughout the lattice of interconnections called gap junctions. The 3D electrical network of cardiomyocytes includes a finer order of complexity that involves a system of deep sarcolemmal membrane invaginations within each cell. As a network within a network, these sarcolemmal invaginations occur transversely with a periodicity roughly corresponding to that of sarcomere *z*-lines (transverse tubules, or T-tubules) and branch in the longitudinal direction (axial tubules) to form a complex system in atrial and ventricular cells, named the transverse-axial tubular system (TATS) (1, 2). The TATS allows membrane potential changes to propagate rapidly into the cardiomyocyte core and is considered an ultimate structural player for excitation–contraction coupling. During rapid depolarization, such as seen during the AP, Ca^{2+} enters the cytosol through depolarization-activated Ca^{2+} channels and triggers further Ca^{2+} release from the sarcoplasmic reticulum through Ca^{2+}-activated ryanodine receptor 2 (RyR2) channels (Ca^{2+}-induced Ca^{2+} release). As a consequence, the free intracellular Ca^{2+} concentration rises, allowing for myofilament activation and contraction (3). Thus, the well-organized topographical extension of surface membrane in T-tubules ensures homogeneous Ca^{2+} release and, consequently, a near-synchronous activation of contraction across each individual cardiomyocyte.

At all levels of complexity of the network (from whole heart to subcellular TATS), the velocity and safety of the spread of excitation depends on both active and passive properties of the individual elements and on their connectivity within the network. Myocardial cell-to-cell conduction has been widely investigated in terms of conduction velocity, space and time constants, and implications for the pathogenesis of arrhythmias. In contrast, the electrical properties of the TATS and how they are affected by structural alterations, such as those occurring in pathology (4, 5), remain largely unknown.

The experimental investigation of membrane electrical properties at subcellular levels is extremely challenging from a technical point of

Significance

The homogenous propagation of the action potential in cardiac cells is guaranteed by a complex network of membrane invaginations called the T-tubular system. In cardiac diseases, T-tubules may show electrical defects that can compromise cell function. Here, we investigate the diffusional properties of fluorescent probes inside T-tubules to predict electrical conductivity of the tubular network. We apply this method to detecting alterations of T-tubule conductivity in a pathological setting characterized by compromised T-tubule integrity. We found that in heart failure, T-tubule conductivity is significantly reduced compared with healthy cardiac cells. A reduction in conductivity can impair the propagation of action potential across the network and may explain the presence of conduction defects found at the single tubular level.

Author contributions: M.S., C.C., C.F., R.C., C.T., E.A.R.-Z., P.K., E.C., C.P., F.S.P., and L. Sacconi designed research; M.S. and L. Sacconi performed research; F.S.P. contributed new reagents/analytic tools; M.S., C.C., T.G., L. Silvestri, and L. Sacconi analyzed data; and M.S., C.C., C.F., T.G., L. Silvestri, R.C., C.T., E.A.R.-Z., P.K., E.C., C.P., and L. Sacconi wrote the paper.

The authors declare no conflict of interest.

This article is a PNAS Direct Submission.

Freely available online through the PNAS open access option.

[1]To whom correspondence should be addressed. Email: sacconi@lens.unifi.it.

This article contains supporting information online at www.pnas.org/lookup/suppl/doi:10.1073/pnas.1702188114/-/DCSupplemental.

view and requires new perspectives. Inspired by geological investigations, in which the diffusional properties of porous rocks have been predicted by electrical data (6), we applied an inverse concept by investigating the diffusional properties of fluorescent probes inside the tubular network to predict TATS electrical conductivity. To do so, TATS diffusional properties are experimentally investigated using fluorescence recovering after photobleaching (FRAP) microscopy (7). Then, considering the TATS as an interconnected system representing an obstacle to free diffusion, we introduced an apparent diffusion coefficient of the fluorescent probe within the network of membrane invaginations. Finally, in view of the formal analogy that exists between diffusion and electrical conduction, the apparent diffusion coefficient is linked to the effective electrical conductivity of the network. The methodology is first validated using an acutely detubulated cellular model (8, 9) and then applied to assessing the effective electrical conductivity in diseased cardiomyocytes where structural (10) and functional (11–15) defects of the TATS have been described.

Results

TATS Diffusion Properties Measured by FRAP Microscopy. Following the pioneering study by Endo (16), T-tubules are labeled using fluorescent dextran (with a nominal molecular mass of 3 kDa) that freely and rapidly diffuses from the extracellular space to the TATS lumen of isolated rat ventricular cardiomyocytes (17). Diffusion of the fluorescent and membrane-impermeable molecule within the TATS lumen allows specific and homogeneous labeling comparable to conventional staining using membrane dyes (Fig. 1*A*). FRAP microscopy is used to investigate the diffusion properties of molecules inside the TATS. First, the whole cell is scanned with a high-power laser to photobleach the fluorescent dextran across the whole cell thickness; then, confocal imaging in a midlevel plane of the cell is used to monitor the diffusion of unbleached dextran from the extracellular space to the TATS (Fig. 1*B*). In confocal microscopy, laser excitation is not axially confined and the bleaching involves the fluorescent dextran inside a probed cell as well as the surrounding solution below and above a cell. To maintain a constant fluorescent dextran concentration in the solution surrounding the probed cell, constant flow is applied during the entire FRAP experiment (Fig. 1*B*). Following the increase in fluorescence intensity inside the lumen of a T-tubule during FRAP (Fig. 1*B*), we found that the fluorescence signal recovers well to the initial level with a mobility fraction $R = 0.77 \pm 0.03$ [$R = (I_\infty - I_0)/(I_i - I_0)$, with I_∞ the fluorescence intensity after full recovery and I_i and I_0 the fluorescence intensity before and just after the bleaching]. The dynamics of recovery at the cell center is characterized by a half-time $t_{½} = 2.4 \pm 0.1$ s. No statistical difference is found in the half-time (at matching spatial observation points) using different concentrations of the 3-kDa dextran, suggesting that the diffusive process of this molecule inside the TATS can be compared with the ideal solution regime (Fig. S1*A*). Using a dextran with a nominal molecular mass of 10 kDa, the hydrodynamic radius of the fluorescent molecule is increased (in accordance with Stoke's law), and $t_{½}$ increases proportionally (by $\sqrt[3]{10\ \text{kDa}/3\ \text{kDa}} \approx 1.5$; Fig. S1*B*) and speed of diffusion in the TATS is reduced.

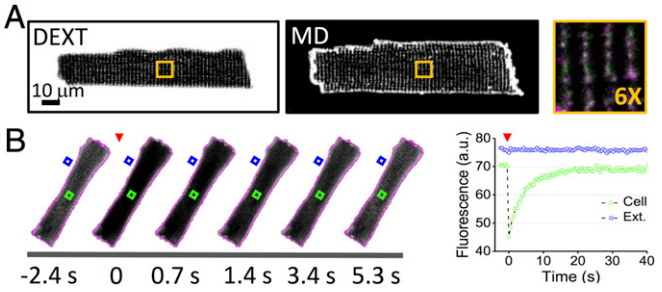

Fig. 1. FRAP microscopy of TATS in rat isolated ventricular myocytes. (*A*) Representative confocal images of a rat cardiomyocyte. (*Left*) TATS lumen is stained with fluorescent dextran (DEXT). (*Middle*) Sarcolemma is stained with di-4-ANBDQPQ (membrane dye, MD). (*Right*) In the orange box is shown a sixfold magnification of the region highlighted in whole-cell images on the left. Fluorescent dextran in green and membrane dye in magenta. (*B*) (*Left*) Sequence of confocal images of a rat cardiomyocyte during FRAP of fluorescent dextran (1 mM, 3 kDa). The fluorescent dextran is photobleached (red arrowhead) by scanning the cell area (whose contour is reported in magenta) with high laser power for 5 s, after which diffusion of unbleached fluorescent dextran from the extracellular space into TATS is monitored. Timeline of the FRAP experiment is reported below. (*Right*) Fluorescence intensity traces corresponding to the cell area indicated by the green box and to the extracellular space highlighted by the blue box. The recording related to the extracellular space (blue box) was performed using a reduced photomultiplier gain avoiding signal saturation. The red arrowhead shows the time of photobleaching. Of note, the cell was perfused with a constant flow of dextran-containing buffer.

To link the characteristic half-time $t_{½}$ with the diffusion coefficient D we need to solve Fick's second law of diffusion using appropriate boundary conditions that are dictated by TATS geometry.

Mathematical Model of Molecular Diffusion in TATS. The idea of solving Fick's second law of diffusion using a deterministic approach faces two main obstacles: (*i*) the lack of a comprehensive model of TATS lumen geometry and (*ii*) the mathematical effort involved in finding the solution itself. Here, inspired by Klinkenberg's porous rock study, we represent a cardiomyocyte and its TATS as a homogenous (at the whole-cell level) entity made up of a complex porous network filled with free diffusing macromolecules. Note that this schematization does not include any access barrier at the cell surface, such as seen in skeletal muscle, because—in line with differences in excitation–contraction-coupling—cardiac T-tubules tend to have wider openings and overall diameters (18–20). With this approach, to circumvent the first obstacle, we can define an apparent diffusion coefficient D' of macromolecules as $D' = D \cdot G$, where G is a dimensionless factor based on the TATS geometry and D is the free diffusion coefficient. To give an idea of G, in a simplified scenario, where the TATS is depicted as an assemblage of straight capillary tubes (Fig. 2*A*), G would be defined as the ratio between the pore (i.e., the T-tubule) cross-sectional area and the total outer surface area (i.e., the surface sarcolemma) and could be written as $G = \sigma \cdot \pi \cdot r_{TT}^2$, where σ is the superficial density of T-tubules and r_{TT} is the T-tubular radius. However, in an actual cardiomyocyte, the "capillaries" are not straight and this increased complexity of the TATS precludes an analytic expression of G, which instead must be experimentally determined.

Let us assume that a cardiomyocyte can be approximated as a porous cylinder (with an average cell radius R_c), in which macromolecules can "freely" diffuse with an apparent diffusion coefficient D'. In this hypothesis, the temporal evolution of the concentration of the fluorescent dextran $\phi\ (t)$ inside the cylinder after photobleaching ($t \geq 0$) can be derived solving Fick's second law of diffusion as follows:

$$\frac{\partial \phi(r,t)}{\partial t} - D'\nabla^2\phi(r,t) = 0 \qquad [1]$$

with the following initial conditions:

$$\phi(r < R_c,\ t = 0) = \phi_0$$

$$\phi(r = R_c,\ t \geq 0) = \phi_i,$$

where r is the radial coordinate (Fig. 2*A*). We assume that during FRAP experiments (*i*) photobleaching produces a uniform fluorescence reduction throughout the cell to ϕ_0 and (*ii*) the concentration of fluorescent dextran at the cell surface remains constant during the entire measurement at ϕ_i. Eq. **1** can be analytically solved (21) as follows:

$$\frac{\phi(r,t)-\phi_0}{\phi_i-\phi_0}=1-\frac{2}{R_c}\sum_{n=1}^{\infty}\frac{\exp\left(-D'\alpha_n^2t\right)\cdot J_0(r\alpha_n)}{\alpha_n\cdot J_1(R_c\alpha_n)}, \quad [2]$$

where α_n are roots of $J_0(R_c\cdot\alpha_n)=0$, and J_0 and J_1 are the zero- and first-order Bessel functions, respectively. Curves showing $\frac{\phi(r,t)-\phi_0}{\phi_i-\phi_0}$ at the center of the cylinder ($r=0$) for different values of D' are plotted in Fig. 2*B*. Alternatively, Fig. 2*C* shows curves of $\frac{\phi(r,t)-\phi_0}{\phi_i-\phi_0}$ at a constant D' for different positions inside the cylinder. The dotted lines in Fig. 2 *B* and *C* show curves obtained considering just the first term of the series in Eq. **2**. We found that the characteristic time (time constant, τ) of fluorescence recovery is independent of the position inside the cylinder and, more generally, that the first term of the series is sufficient to describe the temporal evolution of fluorescence recovery just after the initial phase. The fact that the characteristic time of fluorescence recovery is independent from the position inside the cylinder does not imply that fluorescence recovers simultaneously across the volume. In fact, as evident from Fig. 2*C*, the leading exponential term (the first term of the series) is temporally shifted at different radial values and peripheral regions recover before the central ones, as intuitively expected. Based on these observations, the recovery phases of our FRAP experiments can be fitted using the first series term of Eq. **2**, obtaining a simple exponential equation:

$$\frac{\phi(r,t)-\phi_0}{\phi_i-\phi_0}=1-\frac{2\cdot J_0(r\alpha_1)}{R_c\cdot\alpha_1\cdot J_1(R_c\alpha_1)}\exp\left(-D'\alpha_1^2t\right)=1-C\cdot\exp\left(-t/\tau\right), \quad [3]$$

where C is a time-independent factor and the time constant $\tau=1/\alpha_1^2D'\cong R_c^2/(2.405)^2D'$ where 2.405 is the first root of the zero order of Bessel function (J_0) with four-digit precision. Thus, estimating τ by fitting the experimental FRAP data with Eq. **3** and measuring R_c from confocal images, we can calculate the apparent diffusion coefficient D' that characterizes the whole-cell TATS.

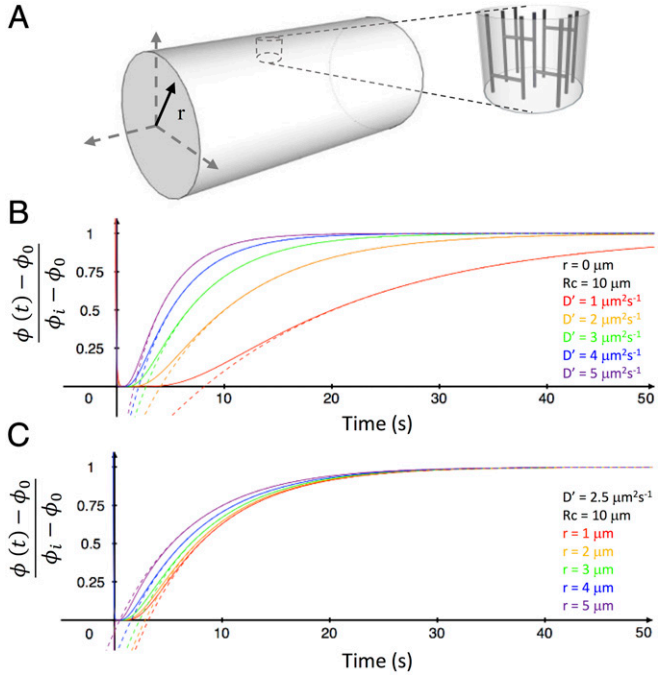

Fig. 2. Mathematical model of molecular diffusion in TATS. (*A*) Cylinder representing a modeled cardiomyocyte with polar coordinate system. The T-tubular system is represented by transverse and axial capillary tubes. (*B*) Plotted curves of the diffusion equation solved in the cylinder Eq. **2** at the center of the cylinder ($r=0$) using different apparent diffusion coefficients (D'). (*C*) Plotted diffusion curves, using $D'=2.5\ \mu m^2\cdot s^{-1}$, solved for different radial positions within the cylinder. Solid lines represent the Eq. **2** mathematical solution and the dotted lines show the solution of the first series term of Eq. **2**: Eq. **3**.

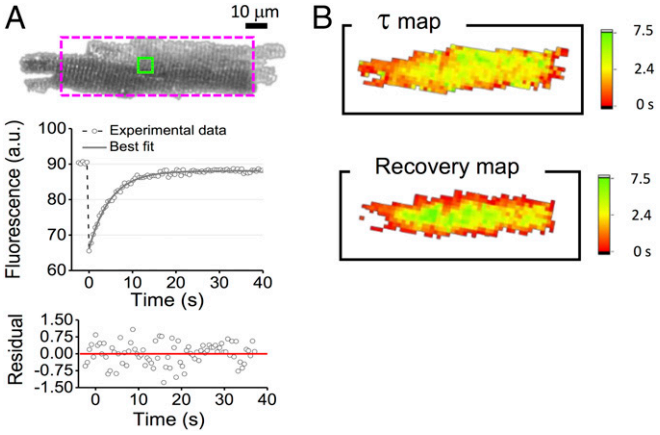

Fig. 3. TATS diffusion properties. (*A, Top*) Representative confocal image of a rat cardiomyocyte, stained with fluorescent dextran. The dotted rectangle represents the best rectangle fitting the cellular area. (*Middle*) FRAP data (gray circles) related to a selected TATS area (green box); the gray line shows the best fit of Eq. **3** to the data. (*Bottom*) Random pattern of the regression residual. (*B*) Color-scaled maps of the diffusion time constant (τ) and the time to recovery of 90% of fluorescence intensity, reporting the corresponding values for each pixel. In these analyses, a 4 × 4 binning was applied to increase the signal-to-noise ratio.

Measuring TATS Apparent Diffusion Coefficient. In agreement with the mathematical model, the fluorescence recovery is described by a pure monoexponential growth (Fig. 3*A*). Using a pixel-by-pixel analysis of the fluorescence recovery we find mild variations of τ across the whole cell, as well as a temporally shifted recovery at different radial values (Fig. 3*B*) in accordance with the predictions of our model. The spatiotemporal behavior of fluorescence recovery was further investigated using a dextran with a nominal molecular mass of 10 kDa. In this case, the higher molecular mass emphasizes the temporal shift between recovery profiles measured at different radial positions within the cell (Fig. S2): We find a temporal shift that is in line with theoretical expectation, confirming the goodness of our mathematical schematization. Cellular radius R_c and the diffusion time constant (τ) were systematically measured in isolated rat cardiomyocytes using 3-kDa fluorescent dextran. Control cardiomyocytes ($n=21$ cells from $N=5$ rats) show $R_c=12.9\pm0.4$ μm and $\tau=4.9\pm0.3$ s; thus, we calculate an apparent diffusion coefficient $D'=6.5\pm0.6\ \mu m^2\cdot s^{-1}$. This is significantly smaller than the free diffusion coefficient $D=145\pm3\ \mu m^2\cdot s^{-1}$ (22), underlining the impact of the TATS in slowing down the diffusion of the dextran in murine ventricular cardiomyocytes. Furthermore, simplifying the TATS geometry as an assembly of straight capillaries, and using published data regarding TATS morphology [$\sigma\approx3\cdot10^7 cm^{-2}$ (23) and $r_{TT}\approx100$ nm (4)] we calculate an apparent diffusion $D'_{Calc}\approx1.4\ \mu m^2\cdot s^{-1}$, which is of the same order of magnitude as the experimentally observed value.

From Apparent Diffusion to Electrical Conductivity. Several physical processes can be quantitatively explored using equations based on formal analogies. In Fick's first law of diffusion, for instance, the diffusion flux is proportional to the concentration gradient ($J=-D\nabla\phi$) The electrical current density j is governed by a similar law ($j=-K\nabla V$), where K is the electrical conductivity and V is the electrical potential difference. Exploiting the formal analogy of these equations, the TATS electrical conductivity K'

may be written as $K' = K \cdot G$, where G is the same dimensionless factor that links the apparent and the free diffusion coefficients. Then, assessing G from FRAP experiments, and measuring the electrical conductivity of the extracellular medium ($0.0120 \pm 0.0002\ \Omega^{-1}\cdot cm^{-1}$; Milwaukee Instruments CD611) we can calculate the TATS electrical conductivity as $K' = (5.3 \pm 0.5)\ 10^{-4}\ \Omega^{-1}\cdot cm^{-1}$. In this calculation, the errors associated to K and D were neglected with respect to the error associated to D'.

Electrical Properties of Acutely Detubulated Cells. To assess the utility of our methodology in probing the electrophysiological consequences of alterations in TATS structure, we physically disconnect T-tubules from the surface sarcolemma of rat healthy cardiomyocytes by using an osmotic shock technique (8). This protocol (acute detubulation) prevents the diffusion of the dextran into disconnected tubules, so that only those elements that are still connected with extracellular space will be fluorescently labeled as a result of dextran diffusion (Fig. 4*A*). Images are then analyzed with a software for automatic detection and analysis of TATS architecture (autoTT; ref. 24). Acute detubulation drastically reduces the number of T-tubules that are continuous with the extracellular space (Fig. 4*B*), while maintaining the cell radius unaltered: $R_c = 13.1 \pm 0.7$ μm. This specific morphological perturbation causes a significant increase in the diffusion time constant (Fig. 4 *A* and *C*) and considerable reductions in TATS diffusion coefficient and TATS conductivity (Fig. 4*D*). Taking into account that the TATS represents a parallel combination of T-tubules, K' is proportional to the number of T-tubules: A reduction of the number of functional tubules will induce a decrease in K'. This result underlines the clear relationship between geometrical and electrical features of the network. For each cell we also performed FRAP analysis in different individual tubules, measuring the recovery characteristic time of each tubule while still bleaching the whole cell. This analysis provided the distribution of τ at single tubular level, from which we could infer the apparent diffusion D', and thus the effective conductivity K', as seen from each single portion of the tubular network (Fig. 4 *E* and *F*). The K' distribution highlights the presence of tubules experiencing an exceptionally low conductivity of the surrounding network. This finding is in line with previous observations where AP propagation failure across TATS was described in acutely detubulated cardiomyocytes (11).

Measuring TATS Conductivity in Failing Hearts. The methodology is applied to measuring TATS properties in cardiomyocytes isolated from aged (15–18 mo old) spontaneously hypertensive rats (SHR) (Fig. 5*A*) with overt heart failure (HF) (25). Loss and disorganization of the TATS (Fig. 5*A* and *B*) are common features of ventricular cardiomyocyte remodeling due to HF in different disease models, including aged SHR rats (5, 11, 26, 27). Ultrastructural modifications, such as increased tubular radius, have been also observed in failing hearts using both electron (28) and super-resolution optical microscopy (4). These morphological alterations can modify TATS electrical conductivity. In fact, as described before, fewer resistive elements in a parallel system could induce a reduction of the global conductivity, whereas the enlargement of individual elements may increase conductivity (23). The net impact of this composite remodeling on electrical conductivity is difficult to predict theoretically, or to assess electrophysiologically. It can be explored, however, by measuring cellular radius $R_c = 13.6 \pm 0.9$ μm and the diffusion time constant at the single tubular level (Fig. 5 *A*, *C*, and *E*). We find that SHR/HF cardiomyocytes are characterized by a significant reduction of the TATS diffusion coefficient and conductivity (Fig. 5 *D* and *F*). As found in the acute detubulation model, the distribution of K' is shifted to lower values, highlighting the presence of tubules experiencing a low network conductivity. In this specific pathological model (SHR/HF), optical measurements of AP at multiple sites within TATS were also performed (Fig. S3), confirming an increase in the presence of tubular elements that fail to depolarize during an AP (Fig. 5*G*).

Discussion

What are the passive electrical properties of the cardiac T-tubular system? How do different TATS structural alterations affect gross electrical conductivity of the network? Addressing these questions has proven to be extremely challenging from a technical point of view and motivated seeking a new perspective. Inspiration came from a geological study (6) in which to assess the diffusive properties of rocks the author investigated their electrical conductivity, thanks to the formal analogy between the two phenomena. Here, picturing ventricular cardiomyocytes as the equivalent of a porous rock, we have reversed this scientific approach and studied diffusion properties of T-tubules to infer electrical properties of the system.

FRAP microscopy has been used to quantify TATS diffusion and, developing a mathematical model, we have linked the time

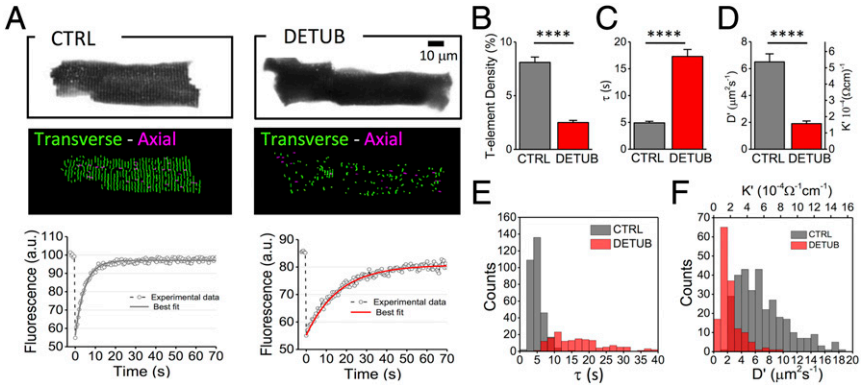

Fig. 4. TATS conductivity in detubulated cardiomyocytes. (*A*, *Top*) Two representative confocal images of control (CTRL) and detubulated (DETUB) rat ventricular cardiomyocytes, stained with fluorescent dextran. (*Middle*) Skeletonized T-tubular system of the top images, obtained with AutoTT (transverse elements in green and axial ones in magenta). (*Bottom*) FRAP data (average from 10 different tubules) from CTRL and DETUB; solid lines show the best fit to data of Eq. **3**. (*B–D*) Graphs showing T-tubular density (determined by dividing number of pixels of T-tubules by the total intracellular area), diffusion time constant (τ), diffusion coefficient (D'), and electrical conductivity coefficient (K'). Data reported as mean ± SEM from $n = 21$ CTRL cells from $N = 5$ rats and $n = 15$ DETUB cells from $N = 4$ rats. (*E* and *F*) Distributions of diffusion time constant (τ), diffusion coefficient (D'), and electrical conductivity coefficient (K') of single T-tubules in CTRL (gray) and detubulated cells (red). Data from 315 T-tubules (CTRL) and 151 T-tubules (DETUB) from $N = 5$ and $N = 4$ rats, respectively. Student's *t* test applied, $^{****}P < 0.0001$.

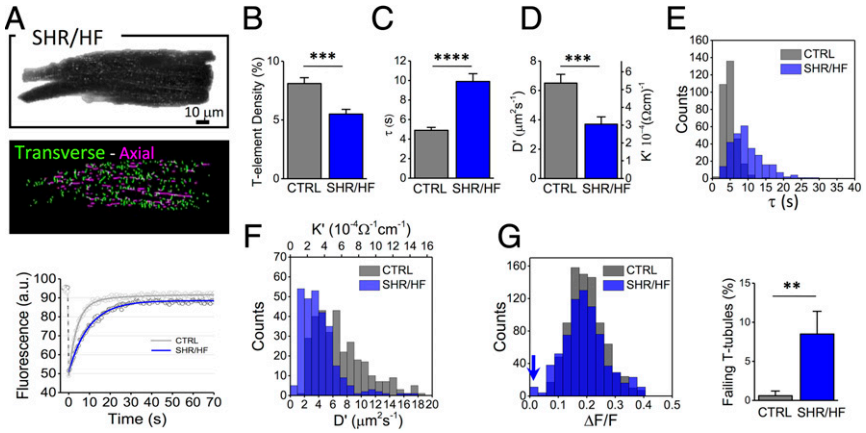

Fig. 5. TATS conductivity in failing hearts. (*A*, *Top*) Representative confocal image of a ventricular cardiomyocyte, isolated from an SHR/HF stained with fluorescent dextran. (*Middle*) Skeletonized T-tubules, obtained with AutoTT (transverse elements in green and axial ones in magenta). (*Bottom*) FRAP data and best fit related to the average of 10 different tubules from CTRL (gray) and SHR/HF (blue) cells. (*B–D*) Graphs showing T-tubular density, diffusion time constant (τ), diffusion coefficient (D'), and electrical conductivity coefficient (K'). Data reported as mean ± SEM from n= 21 cells from $N = 5$ CTRL rats and $n = 19$ cells from $N = 4$ SHR/HF rats. (*E* and *F*) Distributions of diffusion time constant (τ), diffusion coefficient (D'), and electrical conductivity coefficient (K') of single T-tubules in CTRL (gray) and SHR/HF (blue). Data from 315 T-tubules (CTRL) and 279 T-tubules (SHR/HF) from $N = 5$ and $N = 4$ rats, respectively. (*G*) Optical recording of T-tubular AP. The histogram compares the distributions of AP amplitudes recorded in TATS (expressed in ΔF/F) in CTRL and SHR/HF. The blue arrow highlights the presence of T-tubules that fail to depolarize during an AP. Columns showing the percentage of electrically failing T-tubules in CTRL and SHR/HF myocytes. T-tubules are scored as failing elements using the AP threshold of ΔF/F = 0.037 in agreement with previous work (11). Data from 87 T-tubules in $n = 25$ cells, isolated from $N = 8$ CTRL rats and 87 T-tubules in $n = 23$ cells, isolated from $N = 8$ SHR/HF rats. Student's t test applied, $^{**}P < 0.01$, $^{***}P < 0.001$, and $^{****}P < 0.0001$.

constant of fluorescence recovery with the apparent diffusion of molecules inside the T-tubular lumen. Apparent diffusion is used to assess TATS conductivity, which for rats is $K' = (5.3 \pm 0.5)$ 10^{-4} $\Omega^{-1}\cdot cm^{-1}$. Of note, our method operates in a well-defined experimental paradigm where the concentration of fluorescent dextran at the cell surface is maintained constant. Indeed, an unconfined bleaching volume has strong implications on the quantitative assessment of diffusion properties inside the TATS (Fig. S4). It is crucial, therefore, that the extracellular space be agitated in FRAP studies of TATS diffusion, which underlines the importance of constant flow of the extracellular medium during the experiments.

TATS conductivity can be used to evaluate the efficiency of the passive spread of voltage changes along the tubular network. In fact, generalizing the cable theory (29), we can associate with every infinitesimal volume of the tubular system an equivalent electrical circuit based on two factors: r_{TATS}, which is responsible for the voltage drop per unit length due to current flow through the tubular lumen, and r_m, which is responsible for current leakage per unit length across the membrane. Assuming radial current propagation, we can write $r_{TATS} = 1/dS \cdot K'$ and $r_m = R_m/dS \cdot \Sigma$, where dS is the infinitesimal surface perpendicular to the direction of propagation, K' is the TATS conductivity, R_m is the specific resistance per unit area of the membrane, and Σ is the TATS membrane area per unit volume. In this condition, the passive voltage propagation across the TATS decays exponentially with a characteristic length constant $\lambda = \sqrt{r_m/r_{TATS}} = \sqrt{R_m \cdot K'/\Sigma}$. Using published data for $\Sigma = (0.2 \pm 0.1)$ $10^4\cdot cm^{-1}$ (17, 30–32) and $R_m = (3.25 \pm 1.15)$ $k\Omega\cdot cm^2$ (33) and our measured K' we find $\lambda = 290 \pm 90$ μm. This value, in line with prior theoretical models (34), is one order of magnitude larger than the cellular radius, indicating a remarkable safety factor of the normal TATS structure in passively conveying membrane potential changes across the cell: A passive conduction-based drop of only ~4 mV in AP amplitude can be estimated from the surface sarcolemma to the cell core. Although indirect, this is an experimental assessment of the characteristic length constant of the tubular network, having been estimated only theoretically for a long time.

To assess how the TATS conductivity is influenced by geometrical features, we first used acute detubulation to acutely alter the morphology of the TATS, and then we tested our method in detecting alterations of conductivity using myocytes in a pathological setting (i.e., from a rat HF model). We found that a substantial overall reduction of T-tubular density halves the TATS conductivity in both models. However, considering that the length constant is one order of magnitude larger than the cell radius, and that it shows a root dependency on K' and Σ, effective "voltage clamp" across the whole TATS network is assured even if K' and/or Σ change within their respective order of magnitude—as long as sarcolemmal excitability is unchanged (i.e., as long as the whole cell surface is excited nearly synchronously). Ensuring a good electrical coupling of the TATS is essential for propagation of membrane depolarization from the surface to the core of the cell. Measurement of AP propagation in the TATS is a quite recent possibility, achieved by combining random access two-photon microscopy and voltage imaging (11, 35). In line with the above considerations, this methodology revealed that the majority of T-tubules properly propagate the AP, even in diseased cardiomyocytes (11–14). However, these results do not exclude the presence of individual electrically failing tubules. In fact, probing the electrical conductivity at the single tubular level (Figs. 4*F* and 5*F*) highlighted the presence of tubules with low conductivity in detubulated or pathologically remodeled cells.

In conclusion, here we present a methodology to probe electrical conductivity of the cardiac T-tubular system using FRAP. We apply this method to estimating fundamental electrical parameters of healthy cardiac cells as well as of cells with acutely and chronically remodeled TATS. The technique can be used for relatively swift assessments of TATS passive electrical properties at the whole cell level, and for comparison of observations in response to interventions (drugs, pathological signaling mediators, stretch, etc.), as a consequence of disease or therapy effects, and between species.

Methods

Cardiomyocyte Isolation. Ventricular cardiomyocytes from different animal models are isolated by enzymatic dissociation as described before (11). Here we use (*i*) male WKY rats (12 mo old) and (*ii*) SHR with overt HF (SHR/HF, 15–18 mo old). All animal procedures performed conform to the guidelines from Directive 2010/63/EU of the European Parliament on the protection of animals used for scientific purposes; experimental protocol is approved by the Italian Ministry of Health on July 6, 2015 (approved protocol 647/2015-PR).

Acute Detubulation. Isolated cardiomyocytes are gradually readapted to calcium, adding steps of 50 or 100 μM $CaCl_2$ every 5–8 min, until a concentration of 0.5 mM $CaCl_2$ is reached. Detubulation is induced by osmotic shock as previously described (8, 9). Briefly, 1.5 M formamide is added to the cell suspension for 15–20 min; the cells are then resuspended rapidly in standard solution ($CaCl_2$-free).

Cardiomyocyte Labeling. For colocalization experiments, cardiomyocytes are suspended in Tyrode buffer containing fluorescent dextran (dextran, fluorescein, 3 kDa, anionic, lysine-fixable; ThermoFisher Scientific) and 2 μg/mL of di-4-ANBDQPQ (36) (from stock, dissolved in ethanol). Unless otherwise stated, FRAP experiments are performed with 1 mM of 3-kDa fluorescent dextran.

FRAP Technique and Confocal Imaging. FRAP microscopy is performed on dextran-labeled cardiomyocytes. Imaging is performed with a confocal microscope [Nikon Eclipse TE300, with the Nikon C2 scanning head, using the Nikon Plan EPO 60× objective (N.A. 1.4, oil-immersion)]. We acquired images (256 × 256 pixels) at 2.08 frames per second. A 488-nm laser is used for excitation of fluorescein-conjugated dextran. To perform FRAP imaging, an auto-region of interest (ROI) detector is used to recognize the cellular profile. Photobleaching of the fluorescent dextran inside the selected ROI is obtained by increasing the 488-nm laser power for 5 s. The laser power (measured after the objective lens) is 5 μW for imaging and 0.4 mW for photobleaching. Diffusion of unbleached dextran from the outside to the inside of the ROI is monitored using confocal imaging for 70 s. To ensure a constant concentration of fluorescence dextran near the cell surface, a continuous flow of dextran-containing buffer is applied during all phases of FRAP measurements using a piezoelectric micropump (mp6; Bartels Mikrotechnik). Loaded preparations are used for experiments within 30–40 min. Staining and imaging sessions are performed at room temperature (20–22 °C). For colocalization experiments a 561-nm excitation laser is used for di-4-ANBDQPQ–stained cardiomyocytes.

Image Analysis and Statistics. Each FRAP measurement produces a series of confocal images analyzed with a custom-made software written in LabVIEW 2015 (National Instruments) for studying the temporal evolution of fluorescence intensity during bleaching and recovery. Ten to 15 lines (length 2.7 μm) are chosen on 10 different tubules selected across the whole cell and the fluorescence intensity is integrated over line. The fluorescence intensity $I(t)$ is then fitted with an exponential function $I(t) = C'(1 - C \cdot \exp(-t/\tau))$ in accordance with our mathematical model. The best fitted τ values from the 10 lines are used for distribution graphs and averaged within each cell for Student's t test analysis. The radius of cardiomyocytes is estimated using a software written in LabVIEW 2015 (National Instruments). Quantitative analysis of the T-tubule system is obtained by using AutoTT, an automated T-tubule analysis algorithm for confocal images (24).

Data are expressed and plotted as mean ± SEM obtained from different cardiomyocytes. Number of cells (n) and number of animals (N) are indicated in the figure legends for each experimental class. Unpaired Student's t test is used for comparisons. A P value of < 0.05 is considered as indicative of a statistically significant difference between means (**$P < 0.01$, ***$P < 0.001$, ****$P < 0.0001$).

ACKNOWLEDGMENTS. We thank Dr. Marie Caroline Müllenbroich for helpful discussions on the manuscript. This work was supported by European Union's Horizon 2020 research and innovation program Grant 654148 Laserlab-Europe; by the Italian Ministry for Education, University and Research in the framework of the Flagship Project NanoMAX; by Italian Ministry of Health Grant WFR GR-2011-02350583; by Regione Toscana FAS-salute project (Torsade); and by Ente Cassa di Risparmio di Firenze. E.A.R.-Z. and P.K. hold Fellowships from the British Heart Foundation. P.K. acknowledges support by European Research Council Advanced Grant CardioNECT.

1. Brette F, Orchard C (2003) T-tubule function in mammalian cardiac myocytes. *Circ Res* 92:1182–1192.
2. Brandenburg S, et al. (2016) Axial tubule junctions control rapid calcium signaling in atria. *J Clin Invest* 126:3999–4015.
3. Bers DM (2002) Cardiac excitation-contraction coupling. *Nature* 415:198–205.
4. Wagner E, et al. (2012) Stimulated emission depletion live-cell super-resolution imaging shows proliferative remodeling of T-tubule membrane structures after myocardial infarction. *Circ Res* 111:402–414.
5. Lyon AR, et al. (2009) Loss of T-tubules and other changes to surface topography in ventricular myocytes from failing human and rat heart. *Proc Natl Acad Sci USA* 106: 6854–6859.
6. Klinkenberg J (1951) Analogy between diffusion and electrical conductivity in porous rocks. *Geol Soc Am Bull* 62:559–564.
7. Reits EA, Neefjes JJ (2001) From fixed to FRAP: Measuring protein mobility and activity in living cells. *Nat Cell Biol* 3:E145–E147.
8. Kawai M, Hussain M, Orchard CH (1999) Excitation-contraction coupling in rat ventricular myocytes after formamide-induced detubulation. *Am J Physiol* 277: H603–H609.
9. Ferrantini C, et al. (2014) Impact of detubulation on force and kinetics of cardiac muscle contraction. *J Gen Physiol* 143:783–797.
10. Ferrantini C, et al. (2013) The transverse-axial tubular system of cardiomyocytes. *Cell Mol Life Sci* 70:4695–4710.
11. Sacconi L, et al. (2012) Action potential propagation in transverse-axial tubular system is impaired in heart failure. *Proc Natl Acad Sci USA* 109:5815–5819.
12. Crocini C, et al. (2014) Defects in T-tubular electrical activity underlie local alterations of calcium release in heart failure. *Proc Natl Acad Sci USA* 111:15196–15201.
13. Crocini C, et al. (2016) Novel insights on the relationship between T-tubular defects and contractile dysfunction in a mouse model of hypertrophic cardiomyopathy. *J Mol Cell Cardiol* 91:42–51.
14. Crocini C, et al. (2016) T-tubular electrical defects contribute to blunted β-adrenergic response in heart failure. *Int J Mol Sci* 17:E1471.
15. Crocini C, Ferrantini C, Coppini R, Sacconi L (2016) Electrical defects of the transverse-axial tubular system in cardiac diseases. *J Physiol*, 10.1113/JP273042.
16. Endo M (1964) Entry of a dye into the sarcotubular system of muscle. *Nature* 202: 1115–1116.
17. Soeller C, Cannell MB (1999) Examination of the transverse tubular system in living cardiac rat myocytes by 2-photon microscopy and digital image-processing techniques. *Circ Res* 84:266–275.
18. Franzini-Armstrong C, Landmesser L, Pilar G (1975) Size and shape of transverse tubule openings in frog twitch muscle fibers. *J Cell Biol* 64:493–497.
19. Walker SM, Schrodt GR (1965) Continuity of the T system with the sarcolemma in rat skeletal muscle fibers. *J Cell Biol* 27:671–677.
20. Rayns DG, Simpson FO, Bertaud WS (1968) Surface features of striated muscle. I. Guinea-pig cardiac muscle. *J Cell Sci* 3:467–474.
21. Crank J (1975) *The Mathematics of Diffusion* (CPI, Bath, UK).
22. Sandrin D, et al. (2016) Diffusion of macromolecules in a polymer hydrogel: From microscopic to macroscopic scales. *Phys Chem Chem Phys* 18:12860–12876.
23. Pasek M, Simurda J, Christe G (2006) The functional role of cardiac T-tubules explored in a model of rat ventricular myocytes. *Philos Trans A Math Phys Eng Sci* 364: 1187–1206.
24. Guo A, Song LS (2014) AutoTT: Automated detection and analysis of T-tubule architecture in cardiomyocytes. *Biophys J* 106:2729–2736.
25. Song LS, et al. (2006) Orphaned ryanodine receptors in the failing heart. *Proc Natl Acad Sci USA* 103:4305–4310.
26. Wei S, et al. (2010) T-tubule remodeling during transition from hypertrophy to heart failure. *Circ Res* 107:520–531.
27. Guo A, Zhang C, Wei S, Chen B, Song LS (2013) Emerging mechanisms of T-tubule remodelling in heart failure. *Cardiovasc Res* 98:204–215.
28. Ibrahim M, et al. (2012) Mechanical unloading reverses transverse tubule remodelling and normalizes local Ca(2+)-induced Ca(2+)release in a rodent model of heart failure. *Eur J Heart Fail* 14:571–580.
29. Dhein S, et al. (2014) Remodeling of cardiac passive electrical properties and susceptibility to ventricular and atrial arrhythmias. *Front Physiol* 5:424.
30. Page E, McCallister LP, Power B (1971) Sterological measurements of cardiac ultrastructures implicated in excitation-contraction coupling. *Proc Natl Acad Sci USA* 68: 1465–1466.
31. Page E (1978) Quantitative ultrastructural analysis in cardiac membrane physiology. *Am J Physiol* 235:C147–C158.
32. Page E, Surdyk-Droske M (1979) Distribution, surface density, and membrane area of diadic junctional contacts between plasma membrane and terminal cisterns in mammalian ventricle. *Circ Res* 45:260–267.
33. Tseng GN, Robinson RB, Hoffman BF (1987) Passive properties and membrane currents of canine ventricular myocytes. *J Gen Physiol* 90:671–701.
34. Pásek M, Simurda J, Christé G, Orchard CH (2008) Modelling the cardiac transverse-axial tubular system. *Prog Biophys Mol Biol* 96:226–243.
35. Crocini C, Coppini R, Ferrantini C, Pavone FS, Sacconi L (2014) Functional cardiac imaging by random access microscopy. *Front Physiol* 5:403.
36. Matiukas A, et al. (2007) Near-infrared voltage-sensitive fluorescent dyes optimized for optical mapping in blood-perfused myocardium. *Heart Rhythm* 4:1441–1451.